# A Computational Fluid Dynamics Study of Supercritical Antisolvent Precipitation: Mixing Effects on Particle Size

**José Sierra-Pallares**
Departamento de Ingeniería Energética y Fluidomecánica, Universidad de Valladolid, Paseo del Cauce 59 47011 - Valladolid, Spain

Grupo de Procesos a Alta Presión, Departamento de Ingeniería Química. Universidad de Valladolid, Prado de la Magdalena sn. 47011 - Valladolid, Spain

**Daniele L. Marchisio**
Dipartimento di Scienza Materiali e Ingegneria Chimica Politecnico di Torino, C.so Duca degli Abruzzi 24. I-10129 - Torino (Italy)

**María Teresa Parra-Santos**
Departamento de Ingeniería Energética y Fluidomecánica, Universidad de Valladolid, Paseo del Cauce 59 47011 - Valladolid, Spain

**Juan García-Serna**
Grupo de Procesos a Alta Presión, Departamento de Ingeniería Química. Universidad de Valladolid, Prado de la Magdalena sn. 47011 - Valladolid, Spain

**Francisco Castro**
Departamento de Ingeniería Energética y Fluidomecánica, Universidad de Valladolid, Paseo del Cauce 59 47011 - Valladolid, Spain

**María José Cocero**
Grupo de Procesos a Alta Presión, Departamento de Ingeniería Química. Universidad de Valladolid, Prado de la Magdalena sn. 47011 - Valladolid, Spain

*DOI 10.1002/aic.12594*
*Published online April 1, 2011 in Wiley Online Library (wileyonlinelibrary.com).*

*Supercritical fluids have been extensively used for particle production of many natural and pharmaceutical substances providing useful alternatives for pharmaceutical and nutraceutical particulate system formulation. Among the different methods, the gas or supercritical antisolvent (GAS or SAS) process and its variants, have received a considerable interest due to the wide range of materials that can be micronized. Controlling particle formation in order to nucleate small particles is a key issue in GAS and SAS processes and this is directly related to mixing at all scales. In this work, we focus on numerical simulation of the process, emphasizing mixing modeling. Different mixing devices characterized by different nozzles are analyzed, to get an insight into mixing dynamics and its influence on the final particle size distribution. Results show that mixing is determinant in obtaining small*

Correspondence concerning this article should be addressed to J. Sierra-Pallares at jsierra@cfd1.eis.uva.es.

*particles, and that mixing at the microscale is a significant parameter to account for in the proper design of precipitators.* © 2011 American Institute of Chemical Engineers *AIChE J,* 58: 385–398, 2012
*Keywords: crystallization (precipitation), computational fluid dynamics, supercritical processes, turbulence*

## Introduction

Among the existing nanoparticles preparation methods, precipitation by supercritical antisolvent (SAS) is becoming more and more important due to the large amount of chemicals that can be processed with this technology, as witnessed by the number of articles reported in the literature.[1–3] There are two possible precipitation mechanisms considered in the antisolvent processes, namely the drop dispersion followed by mass transfer between the droplet and the supercritical fluid, and micromixing with the supercritical fluid.[4] Above the mixture critical point, complete miscibility conditions exist, typically in the range 9–15 MPa, $CO_2$ is completely miscible with many organic solvents[3] and turbulent supercritical mixing is the most relevant issue.

Although the mixing effects on precipitation are well-known for liquid-based systems,[5] such effects are not very often reported in supercritical systems. The supercritical antisolvent process involves the mixing of two streams in a nozzle, to get the desired thermodynamic conditions to produce supersaturation and particle formation. This process is not very different from mixing of two liquid solutions, and the resulting particle size distribution (PSD) is affected by mixing also for supercritical fluids.[6]

While there are a number of studies supporting this evidences from the experimental point of view, little research is available in the framework of numerical modeling. A mathematical model for mass transfer between a droplet of organic solvent and a compressed antisolvent was developed by Werling and Debenedetti,[7] whereas Chávez et al. propose a methodology to calculate the time scales involved in the process.[8] A more elaborated model, solved by computational fluid dynamics (CFD), was proposed by Martín and Cocero.[9] In that research, a turbulence model was solved in conjuction with mass balances to take into account the effect of mass transfer in the system. The authors employed an interpolative closure to solve the population balance equations (PBE).[10] The results were strongly affected by the value of a key parameter (i. e., the surface solid-fluid tension). Predictions obtained with the model are valuable to understand the behavior of the process and to scale it up to the industrial level.

Henczka et al.[11] studied numerically the supercritical antisolvent precipitation of paracetamol with carbon dioxide as antisolvent. Mass, momentum, and energy balances to take into account the heat of mixing in the studied system were solved with the commercial CFD code FLUENT(R). The PSD was calculated using the standard method of moments, and the interaction between mixing and precipitation was taken into account with the $\beta$- PDF approach coupled with the turbulent mixer model of Baldyga.[12] This first attempt showed the importance of including mixing effects in the model, and highlighted some limitations of the available approaches.

It is particularly interesting to mention here that the micromixing models available in the literature, which are necessary to account for the interactions between turbulence and particle formation are only valid for standard fluids, and their extension to supercritical fluids is not straightforward. It is well known that the properties of fluids change dramatically near and above the critical point, therefore, the fluid-dynamic behavior also changes[13] and this directly influences mixing at all scales.

In this work, we present a complete methodology to model precipitation systems in supercritical fluids with a dramatic change in the Schmidt number. The aim of this work is to provide a mathematical formulation capable of describing the turbulent mixing phenomena observed in the SAS process. Once validated, this method can be used for the modeling, scale-up and optimization of these systems, with acceptable accuracy for engineering calculations.

The work is organized as follows: Section 2 presents the complete model, emphasizing the turbulent mixing model. Section 3 deals with the test cases used to validate the model. In Section 4, the validation of the model and the main results found are presented.

## Governing Equations

In this section, the main features of the model are described as mentioned above. First, thermodynamic modeling is commented, secondly the governing equations, concerning mass, momentum, species, and energy balances are considered, including the turbulence closures employed. The description of a micromixing model specially suited to deal with supercritical fluids follows, and the section ends with the description of the population balance equations and the calculation methods for molecular transport properties.

### *Thermodynamic modelling*

In this work, the well-known Peng - Robinson equation of state modified by Stryjek and Vera (PRSVEOS)[14] is employed. The choice is based on in its wide application to the SAS process[9,15] and its succesful application in CFD calculations of other particulate processes at supercritical conditions.[16] Its relative simple form is also very suitable for its use in CFD:

$$p = \frac{RT}{v - b_m} - \frac{a_m}{v(v + b_m) + b_m(v - b_m)}, \tag{1}$$

where $p$ is the thermodynamic pressure, $v$ is the molar volume, $T$ is the temperature, and $a_m$ and $b_m$ are the parameters of the PRSVEOS.

The mixing rule proposed by Wong and Sandler[17] is used to extend the PRSVEOS to mixtures. This rule can predict the high pressure behavior of the mixture without

Correspondence concerning this article should be addressed to J. Sierra-Pallares at jsierra@cfd1.eis.uva.es

considerable loss of accuracy.[18] Besides, the rule has demonstrated to be quite accurate in modelling the heat of mixing in binary systems involving supercritical components.[19] In particular, the parameters $a_m$ and $b_m$ are calculated as follows:

$$b_m = \frac{RT\sum_k\sum_l\left(b-\frac{a}{RT}\right)_{kl}}{RT-\left[\sum_k Y_k\frac{a_k}{b_k}+\frac{G^{ex}}{C^\star}\right]}, \tag{2}$$

$$a_m = b_m RT\left[\sum_k Y_k\frac{a_k}{b_k}-\frac{G^{ex}}{C^\star}\right], \tag{3}$$

with

$$\left(b-\frac{a}{RT}\right)_{kl}=\frac{b_k+b_l}{2}-\frac{\sqrt{a_k a_l}}{RT}(1-\mathbb{K}_{kl}), \tag{4}$$

where,

$$a_k = 0.457235\times\frac{R^2T_{c,k}^2}{P_{c,k}}\alpha_k(T), \tag{5}$$

$$b_k = 0.077796\times\frac{RT_{c,k}}{P_{c,k}}, \tag{6}$$

where $\mathbb{K}_{kl}$ is the binary interaction parameter of species $k$ and $l$; $Y_k$ the molar composition of species $k$ and subindex $c$ correspond to critical properties. The constant $C^{\star} = [\ln(\sqrt{2}-1)]/\sqrt{2} = 0.62323$ for the Peng-Robinson equation of state. $\alpha_i(T)$ is defined as follows:

$$\alpha_i(T) = \left[1+\kappa(1-\sqrt{T_{ri}})\right]^2. \tag{7}$$

Stryjek and Vera modified the temperature dependence of the $\alpha_i(T)$ term,

$$\kappa = \kappa_0+\kappa_1\left(1+\sqrt{T_R}\right)(0.7-T_R), \tag{8}$$

with $\kappa_0 = 0.378893 + 1.4897153\omega - 0.17131848\omega^2 + 0.0196554\omega^3$; where $\omega$ is the acentric factor, $T_R$ is the reduced pressure and $\kappa_1$ is a constant that depends on the substance.

In these equations, $G^{ex}$, the molar excess Gibbs free energy obtained from any excess free energy model, is a function of temperature and composition only. In this article, the well known Non-Random Two-Liquid activity coefficient model (NRTL)[20] has been used to calculate $G^{ex}$. Further details are given elsewhere[21]

Since the PRSVEOS equation of state is not able to represent the behavior of solid phases, the fugacity of the solid is obtained from the fugacity of a reference sub-cooled liquid with the following equation[15]:

$$\varphi^S = \varphi^L\exp\left(\int_{p_0}^{p}\frac{v^S-v^L}{RT}\,dP+\frac{\Delta H_F}{T}\left[\frac{1}{T_f}-\frac{1}{T}\right]\right), \tag{9}$$

where $\varphi$ is the fugacity, $p_0$ is a reference pressure, superscript $S$ and $L$ refer to solid and liquid phases respectively and $\Delta H_F$ is the melting enthalpy of the solid. It is possible to simplify this equation by neglecting the first addendum of the exponential term, because the difference between solid and liquid molar volumes is usually very small.

### *Fluid dynamic model*

The flow and mixing of fluids under supercritical conditions are governed by fundamental conservation equations for mass, momentum, species, and energy.[22] When dealing with turbulent flows, a suitable averaging method must be used. The density averaging technique (or Favre averaging)[23] derives a time-averaged solution by using an average value and fluctuation to replace actual flow parameter values. The complete equations in mass-weighted variables become, neglecting Soret and Dufour effects:

$$\frac{\partial\bar{\rho}}{\partial t}+\partial\frac{(\bar{\rho}\tilde{u}_j)}{\partial x_j}=0, \tag{10}$$

$$\frac{\partial(\bar{\rho}\tilde{u}_i)}{\partial t}+\frac{\partial}{\partial x_j}(\bar{\rho}\tilde{u}_j\tilde{u}_i) = -\frac{\partial\tilde{p}}{\partial x_i}+\frac{\partial}{\partial x_j}\left(\tilde{\sigma}_{ij}-\bar{\rho}\widetilde{u_i''u_j''}\right)+\bar{\rho}g_i, \tag{11}$$

$$\frac{\partial(\bar{\rho}\tilde{e})}{t}+\frac{\partial}{\partial x_j}\left(\bar{\rho}\tilde{u}_j\left[\tilde{e}+\frac{\tilde{p}}{\bar{\rho}}\right]\right) = \frac{\partial}{\partial x_j}\left[\lambda\frac{\partial\tilde{T}}{\partial x_j}+\tilde{u}_j\left(\tilde{\sigma}_{ij}-\bar{\rho}\widetilde{u_i''u_j''}\right)-\right.$$
$$\left.-\bar{\rho}\widetilde{e''u_j''}+\bar{\rho}\hat{h}_k\left(\mathcal{D}\frac{\partial\tilde{Y}_k}{\partial x_j}-\widetilde{Y_k''u_j''}\right)\right], \tag{12}$$

$$\frac{\partial(\bar{\rho}\tilde{Y}_k)}{\partial t}+\frac{\partial}{\partial x_j}(\bar{\rho}\tilde{u}_j\tilde{Y}_k) = \frac{\partial}{\partial x_j}\left[\bar{\rho}\mathcal{D}\frac{\partial\tilde{Y}_k}{\partial x_j}-\bar{\rho}\widetilde{Y_k''u_j''}\right], \tag{13}$$

where $u_j$ is the velocity component in the $x_j$ direction; $\rho$ is the density; $e$ is the internal energy; $\hat{h}_k$ is the partial mass enthalpy of species $k$; $\mathcal{D}$ is the mass diffusivity; $\lambda$ is the thermal conductivity and $g_i$ is the gravitational acceleration in the $x_i$ direction. The viscous stress tensor, $\sigma_{ij}$, reads as follows:

$$\tilde{\sigma}_{ij} = \eta\left[\left(\frac{\partial\tilde{u}_i}{\partial x_j}+\frac{\partial\tilde{u}_j}{\partial x_i}\right)-\frac{2}{3}\delta_{ij}\frac{\partial\tilde{u}_k}{\partial x_k}\right], \tag{14}$$

where $\eta$ is the molecular viscosity. In this work, the Reynolds stress tensor $-\overline{\rho u_i'' u_j''}$ is calculated with the well-known k $-$ $\epsilon$ Realizable model,[24] that has been successfully employed in the description of turbulent supercritical jets at low Reynolds number.[25] The unclosed terms are calculated as follows:

$$-\widetilde{Y_k''u_j''} = \mathcal{D}^T\frac{\partial\tilde{Y}_k}{\partial x_j} \qquad \text{with} \qquad \mathcal{D}^T=\frac{\eta_T}{\bar{\rho}\mathrm{Sc}^T}. \tag{15}$$

where $\mathcal{D}^T$ is the turbulent diffusivity; $\eta^T$ is the turbulent viscosity and $\mathrm{Sc}^T$ is the turbulent Schmidt number, which is fixed to a value of 0.7.[12] In the energy equation,

$$-\bar{\rho}\widetilde{e''u_j''} = \lambda^T\frac{\partial\tilde{T}}{\partial x_j} \qquad \text{with} \qquad \lambda^T=\frac{C_p\eta^T}{\mathrm{Pr}^T} \tag{16}$$

where $\lambda^T$ is the turbulent conductivity; $C_P$ is the constant pressure heat capacity, calculated with the PRSVEOS and zero-pressure heat capacities and $\mathrm{Pr}^T$ is the turbulent Prandtl number, taken equal to 0.85 in this work.

### *Mixing models*

In a supercritical antisolvent crystallization system, a very fast process generates an insoluble product that, due to high supersaturation conditions, precipitates in a particulate solid phase. The resulting PSD is affected by the relative rates of nucleation, growth, and aggregation.[26] The final product quality of crystallization and precipitation processes is often determined by the interplay between mixing and these three phenomena.[5,27] Moreover, when precipitation occurs on a time-scale comparable with that of mixing, a model capable of describing the interactions between turbulent fluctuations and particle formation is needed. In this research, a micromixing model is used to account for these interactions. It is based on the direct quadrature method of moments (DQMoM) coupled with the interexchange with the mean (IEM) model.[28] The model has been validated for turbulent reacting liquid flows.[29] The model is not limited to liquids and can be easily adapted to processes involving supercritical fluids.

DQMoM-IEM is a presumed probability function (PDF) approach that assumes that the joint-composition PDF is constituted by a summation of a finite number $N_e$ of delta functions.[30] Each delta function represents a reacting "environment," characterized by its probability, $\mathcal{P}_n(\mathbf{x},t)$, and the local composition value. Solvent displacement process are often described in terms of a non reacting scalar, called the mixture fraction $\xi$. In the DQMoM-IEM representation, each environment will be characterized by a local mixture fraction value $\xi_n$. When a number of environments ($N_e$) equal to two is chosen, the micromixing model (for the mixture fraction) must solve three transport equations. The first one is the transport equation relative to the probability of the first environment $\mathcal{P}_1$:

$$\frac{\partial(\bar{\rho}\mathcal{P}_1)}{\partial t}+\frac{\partial}{\partial x_j}\left(\bar{\rho}\tilde{u}_i\mathcal{P}_1-\bar{\rho}\mathcal{D}^T\frac{\partial\mathcal{P}_1}{\partial x_j}\right)=0, \tag{17}$$

whereas the probability of the second environment can be computed as

$$\mathcal{P}_2=1-\mathcal{P}_1, \tag{18}$$

because by definition, the probabilities $\mathcal{P}_n$ sum to unity (as the PDF integrates to one). The second and third transport equations are those for the mixture fraction in the first and second environment:

$$\frac{\partial(\mathcal{P}_1\xi_1)}{\partial t}+\frac{\partial}{\partial x_j}\left(\bar{\rho}\tilde{u}_i\mathcal{P}_1\xi_1-\bar{\rho}\mathcal{D}^T\frac{\partial\mathcal{P}_1\xi_1}{\partial x_j}\right)=\bar{\rho}\gamma\mathcal{P}_1\mathcal{P}_2[\xi_2-\xi_1]+\frac{\bar{\rho}\mathcal{D}^T}{\xi_1-\xi_2}\left(\mathcal{P}_1\frac{\partial\xi_1}{\partial x_j}\frac{\partial\xi_1}{\partial x_j}+\mathcal{P}_2\frac{\partial\xi_2}{\partial x_j}\frac{\partial\xi_2}{\partial x_j}\right), \tag{19}$$

$$\frac{\partial(\bar{\rho}\mathcal{P}_2\xi_2)}{\partial t}+\frac{\partial}{\partial x_j}\left(\bar{\rho}\tilde{u}_i\mathcal{P}_2\xi_2-\bar{\rho}\mathcal{D}^T\frac{\partial\mathcal{P}_2\xi_2}{\partial x_j}\right)=\bar{\rho}\gamma\mathcal{P}_1\mathcal{P}_2[\xi_1-\xi_2]+\frac{\bar{\rho}\mathcal{D}^T}{\xi_2-\xi_1}\left(\mathcal{P}_1\frac{\partial\xi_1}{\partial x_j}\frac{\partial\xi_1}{x_j}+\mathcal{P}_2\frac{\partial\xi_2}{\partial x_j}\frac{\partial\xi_2}{\partial x_j}\right), \tag{20}$$

It is interesting to remind here that this representation of the system is very convenient, because it reduces the number of equations to solve. The mixture fraction is a nonreacting scalar bounded between zero and one that defines the amount of fluid coming from one inlet with respect to other one. In this work, the mixture fraction corresponds to the solvent mass fraction in the computational domain and its calculation suffices for the calculation of many interesting scalar quantities, such as the amount of nanoparticle precursor in the solvent. This point will become clearer in the next paragraphs of this section.

The mean mixture fraction is defined as:

$$\tilde{\xi}=\mathcal{P}_1\xi_1+\mathcal{P}_2\xi_2, \tag{21}$$

and defines the degree of mixing at the macroscale through the Large Scale Segregation (LSS) and Small Scale Segregation (SSS). LSS is defined as:

$$\mathrm{LSS}=\left(\tilde{\xi}-\langle\xi\rangle\right)^2, \tag{22}$$

where $\langle\xi\rangle$ is the value of the mean mixture fraction when mixing is complete. The mixture fraction variance is instead defined as:

$$\widetilde{\xi''^2}=\mathcal{P}_1\xi_1^2+\mathcal{P}_2\xi_2^2-\tilde{\xi}^2. \tag{23}$$

It is a measure of the extent of mixing at the microscales and is also known as Small Scale Segregation (SSS). It is also possible to directly derive a transport equation for the mixture fraction variance $\widetilde{\xi''^2}$ resulting in what follows:

$$\frac{\partial(\bar{\rho}\widetilde{\xi''^2})}{\partial t}+\frac{\partial}{\partial x_j}\left(\bar{\rho}\tilde{u}_i\widetilde{\xi''^2}-\bar{\rho}\mathcal{D}^T\frac{\partial\widetilde{\xi''^2}}{\partial x_j}\right)=2\bar{\rho}\mathcal{D}^T\frac{\partial\tilde{\xi}}{\partial x_j}\frac{\partial\tilde{\xi}}{\partial x_j}-2\bar{\rho}\gamma\widetilde{\xi''^2}. \tag{24}$$

As explained by Liu and Fox,[28] the generation term of Eq. 24 corresponds to the rate of dissipation of the LSS. After reactants are fed separately inside the reactor-mixer, LSS is transported to smaller time- and length-scales thanks to turbulent diffusion and generates the small-scale variance (SSS), that finally is dissipated due to molecular mixing.

In Eqs. 19, 20, and 24, $\gamma$ is the micromixing rate, defined as follows

$$\gamma=C_\phi\frac{\tilde{\varepsilon}}{2\tilde{k}_{\mathrm{turb}}}, \tag{25}$$

where $\tilde{\varepsilon}$ is the turbulence dissipation rate; $\tilde{k}_{\mathrm{turb}}$ is the turbulent kinetic energy and $C_\phi$ is known as the mechanical to scalar time ratio. In general, $C_\phi$ is a function of the Schmidt number, Sc:

$$\mathrm{Sc}=\frac{\eta}{\rho\mathcal{D}}, \tag{26}$$

and the local Reynolds number:

$$\mathrm{Re}_l = \frac{\tilde{k}_{\mathrm{turb}}}{\sqrt{\tilde{\varepsilon}\nu}}, \tag{27}$$

where $\nu$ is the kinematic viscosity. In the literature, it is possible to find expressions for $C_\phi$ as a function of $\mathrm{Re}_l$.[28] Unfortunately, those expressions are developed for fixed values of the Schmidt number. In the SAS process, a pressurized solvent (i. e., an organic solvent) is mixed with supercritical carbon dioxide, resulting in a change for the Schmidt number from values close to 300 to typical values of supercritical mixtures ($\approx 5$). This strong change must be taken into account in the calculation of $C_\phi$ to blackcorrectly predict the micromixing rate in the SAS process. To do such thing, it is necessary to integrate over the scalar and turbulent energy spectrum.[31] In this work, we have followed the methodology of Fox[30] to calculate $C_\phi$ as a function of Sc and $\mathrm{Re}_l$ in Eq. 25 and the final dependence is shown in Figure 1.

### *Population balance*

In this work, the Quadrature Method of Moments (QMoM) is employed to track the evolution of the lower order moments of the PSD. The population balance equation (PBE) describes how the population of particles evolves due to nucleation, molecular growth, and aggregation. In the QMoM paradigm, the closure problem is overcome by using a quadrature approximation.[32] The Favre averaged moment of order $\ell$ of the PSD is defined as:

$$\widetilde{\mathcal{M}^\ell} = \int_0^{+\infty} \tilde{n}(L;\ \mathbf{x},\ t) L^\ell \, d\ell = \mathcal{P}_1 \mathcal{M}_1^\ell + \mathcal{P}_2 \mathcal{M}_2^\ell, \tag{28}$$

where $\tilde{n}(L;\mathbf{x}, t)$ is the Favre averaged PSD; $L$ is the particle size and $\mathcal{M}_1^\ell$ and $\mathcal{M}_2^\ell$ are the $\ell$th moments in environments 1 and 2, respectively. Using the quadrature approximation, it is possible to write Eq. 28 as follows:

$$\mathcal{M}_n^\ell \approx \sum_{i=1}^{N} w_{i,n} L_{i,n}^\ell, \tag{29}$$

where $w_{i,n}$ are the weights and $L_{i,n}$ are the abscissas of the $N$ nodes of the quadrature approximation in environment $n$ calculated from the moments through the so-called product - difference algortihm. By choosing two nodes for the quadrature approximation of moments ($N = 2$), it is possible to correctly predict the moments up to the third order.[33] The following equations for the generic moment of order $\ell = 0$, 1, 2, 3 are obtained by applying the moment transformations to the PBE in each environment:

$$\begin{aligned}
\frac{\partial(\bar{\rho}\mathcal{M}_1^\ell)}{\partial t} + \frac{\partial}{\partial x_j}\left(\bar{\rho}\tilde{u}_i \mathcal{M}_1^\ell - \bar{\rho}\mathcal{D}^T \frac{\partial \mathcal{M}_1^\ell}{\partial x_j}\right) &= \bar{\rho}\gamma \mathcal{P}_1 \mathcal{P}_2 \left[\mathcal{M}_2^\ell - \mathcal{M}_1^\ell\right] \\
&+ \frac{\bar{\rho}\mathcal{D}^T}{\mathcal{M}_1^\ell - \mathcal{M}_2^\ell}\left(\mathcal{P}_1 \frac{\partial \mathcal{M}_1^\ell}{\partial x_j}\frac{\partial \mathcal{M}_1^\ell}{\partial x_j} + \mathcal{P}_2 \frac{\partial \mathcal{M}_2^\ell}{\partial x_j}\frac{\partial \mathcal{M}_2^\ell}{\partial x_j}\right) \\
&+ \bar{\rho}\Bigg\{(x_{c,1})^\ell J(S_1) + \ell \sum_{i=1}^{N} G(S_1, L_{i,1}) w_{i,1} L_{i,1}^{\ell-1} \\
&+ \sum_{i=1}^{N} w_{i,1} \sum_{j=1}^{N} w_{j,1} (L_{i,1}^3 + L_{j,1}^3)^{\ell/3} \beta_{\mathrm{agg}}(L_{i,1}, L_{j,1}) \\
&- \sum_{i=1}^{N} w_{i,1} L_{i,1}^k \sum_{j=1}^{N} w_{j,1} \beta_{\mathrm{agg}}(L_{i,1}, L_{j,1})\Bigg\},
\end{aligned} \tag{30}$$

$$\begin{aligned}
\frac{\partial(\bar{\rho}\mathcal{M}_2^\ell)}{\partial t} + \frac{\partial}{\partial x_j}\left(\bar{\rho}\tilde{u}_i \mathcal{M}_2^\ell - \bar{\rho}\mathcal{D}^T \frac{\partial \mathcal{M}_2^\ell}{\partial x_j}\right) &= \bar{\rho}\gamma \mathcal{P}_1 \mathcal{P}_2 \left[\mathcal{M}_1^\ell - \mathcal{M}_2^\ell\right] \\
&+ \frac{\bar{\rho}\mathcal{D}^T}{\mathcal{M}_2^\ell - \mathcal{M}_1^\ell}\left(\mathcal{P}_1 \frac{\partial \mathcal{M}_1^\ell}{\partial x_j}\frac{\partial \mathcal{M}_1^\ell}{\partial x_j} + \mathcal{P}_2 \frac{\partial \mathcal{M}_2^\ell}{\partial x_j}\frac{\partial \mathcal{M}_2^\ell}{\partial x_j}\right) \\
&+ \bar{\rho}\Bigg\{(x_{c,2})^\ell J(S_2) + \ell \sum_{i=1}^{N} G(S_2, L_{i,2}) w_{i,2} L_{i,2}^{\ell-1} \\
&+ \sum_{i=1}^{N} w_{i,2} \sum_{j=1}^{N} w_{j,2} (L_{i,2}^3 + L_{j,2}^3)^{\ell/3} \beta_{\mathrm{agg}}(L_{i,2}, L_{j,2}) \\
&- \sum_{i=1}^{N} w_{i,2} L_{i,2}^k \sum_{j=1}^{N} w_{j,2} \beta_{\mathrm{agg}}(L_{i,2}, L_{j,2})\Bigg\}.
\end{aligned} \tag{31}$$

The right hand side reports the terms describing micromixing, spurious correction, nucleation, molecular growth ($G$) and finally birth and death terms due to aggregation. $S_n$ is the supersaturation in the $n$ environment; $x_{c,n}$ is the size of newly formed particles; $J$ is the nucleation rate and $\beta_{\mathrm{agg}}$ is the aggregation kernel.[29] The functional form of these rate functions will be given in the next section.

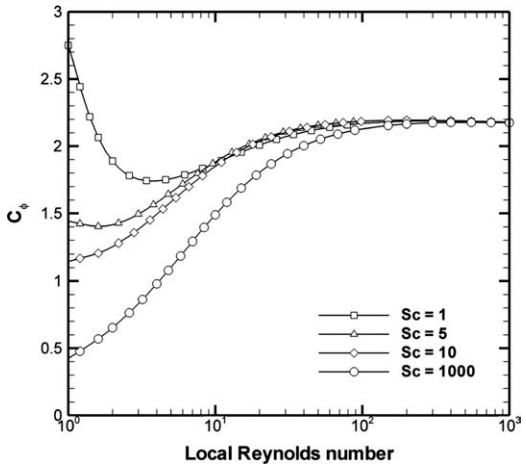


**Figure 1. Pressure - composition diagram for the system $CO_2$ - Dichloromethane at 311.5 K calculated with the PRSVEOS and the Wong-Sandler mixing rule. Experimental data taken from Ref. 47.**

### *Precipitation kinetics*

Particle formation in supercritical fluids occur as result of rapid increase of supersaturation either by means of expansion[34] or by antisolvent mixing[35] process. Supersaturation is the driving force for precipitation and is defined as:

$$S_n = \frac{c_{s,n}}{c_{s,eq}}, \tag{32}$$

where $c_{s,n}$ is the solute concentration in environment $n$ and $c_{s,eq}$ is the equilibrium concentration calculated from the PRSVEOS and the Wong-Sandler mixing rule[36]

As it is reported above, we avoid the solution of the mass balance equation by resorting to the mixture fraction. In fact, the solute is initially dissolved in the solution stream and there is no chemical reaction, a simple mass balance statement results in the following equation[37]:

$$c_{s,n} = \frac{c_{s,0}}{M_w}\xi_n - \frac{\rho_s}{M_w}\frac{\pi}{6}\mathcal{M}_n^3 \tag{33}$$

where $\rho_s$ is the solute density, $c_{s,0}$ is the concentration of solute in the solvent stream and $M_w$ is the solute molecular weight. The physical meaning of $\mathcal{M}_n^3$ is the total volume of particles produced per volume of the solid-fluid mixture in each environment. The shape factor ($\pi/6$) is taken as for spherical particles for simplification.

In this work, it is assumed that the particles are formed by homogeneous nucleation[38] according to the following rate:

$$J(S_n) = 1.5\mathcal{D}\left[c_{s,eq}S_nN_A\right]^{7/3} \times \sqrt{\frac{\sigma_s}{k_BT}}v_{s,m}\exp\left(-\frac{16\pi}{3}\left[\frac{\sigma_s}{k_BT}\right]^3\frac{v_{s,m}^2}{\ln^2(S_n)}\right), \tag{34}$$

where $N_A$ is the Avogadro number; $\sigma_s$ is the surface tension; $k_B$ is the Boltzmann constant; and $v_{s,m}$ is the molecular volume of the solute. Due to the functional form of the above equation, nucleation is strongly dependent on the value of the surface tension. Since this parameter is not known for the analyzed system, it is taken as a fitting parameter in this work. Concerning molecular growth, due to high the supersaturation conditions, diffusion of the bulk solution is the main mechanism of growth. The growth rate is[38]:

$$G(S_n, L_{i,n}) = 2\mathrm{Sh}\frac{M_w}{\rho_p}\frac{\mathcal{D}}{L_{i,n}}c_{s,eq}(S-1), \tag{35}$$

where $\rho_s$ is the solute density and Sh is the Sherwood number. Since there is no relative motion between the particles and the surrounding fluid, Which means a small relaxation time, it is assumed that Sh = 2. However, there can be an effect of fluid deformation [39] as a direct effect of ambient vorticity. It is possible to derive a simple criteria to neglect hydrodynamics effects[40]:

$$\mathrm{Sh} = 2 + \mathcal{A}\mathrm{Re_p}^{3/4}\mathrm{Sc}^{1/2}, \tag{36}$$

where $\mathcal{A}$ is a constant and $\mathrm{Re}_p$ is the particle Reynolds number. The last term of the right-hand side of the equation vanishes at the conditions presented in this work, since the particles are very small. Aggregation of nano-particles is dominated by Brownian motions and therefore their collision frequency $\beta_{\mathrm{agg}}$ can be easily calculated as:

$$\beta_{\mathrm{agg}} = \frac{2k_BT}{3\mu}\frac{\left(L_{i,n}+L_{j,n}\right)^2}{L_{i,n}L_{j,n}}. \tag{37}$$

### *Transport property models*

In this work, molecular viscosity and thermal conductivity have been evaluated by the method proposed by Chung et al.[41] To model diffusion coefficients, the correlation of He and Yu is employed.[42]

## Test Cases, Operating Conditions, and Numerical Details

Since the aim of this research is to investigate the effects of mixing in the SAS process, the work of Cocero et al.[43] has been chosen as a benchmark to validate the model. This work focuses on an experimental device that consists on a tubular precipitator of 40 cm long and 8 cm in diameter placed vertically. The entries of fluids consist on a coaxial nozzle. A sketch of the device with key measures is presented in Figure 3. The system studied was the precipitation of $\beta$-carotene with carbon dioxide as antisolvent and dichloromethane as solvent using the SAS process. In that research, results of particle size obtained with nozzles of different sizes ($D$ = 1 mm and 100 $\mu$m) are presented. The choice of this data set is justified, because it explores two different mixing nozzles, resulting in different mixing patterns. Details regarding the experimental characterization of particle diameter can be found elsewhere.[44–46] Table 1 summarizes the experimental conditions investigated. Under these conditions, there exists a complete miscibility between $CO_2$ and dichloromethane. As already mentioned in the introduction, turbulent mixing between the solvent and the antisolvent occurs in a single phase for all compositions. Figure 2 shows a pressure - composition diagram of the system $CO_2$ - dichloromethane where operating conditions are indicated.

### *Computational details*

Simulations were run on a two-dimensional axisymmetric computational geometry. Different grid models of 5 $\times$ $10^3$, 50 $\times$ $10^3$, and 150 $\times$ $10^3$ cells were tested. In the last cases, the averaged flow obtained is independent of grid resolution. In all the cases, the $y^+$ value is lower than four at the computational walls. A segregated solver was selected, the pressure velocity coupling problem was solved with the SIMPLE approach and first order schemes were used for spatial discretization. The

**Table 1. Experimental Data Set Taken from Ref. 43**

| Case | Nozzle | $T$ (K) | $p$ (bar) | $c_0$ ppm | $F_{CO2}$ (kg h$^{-1}$) | $F_{\mathrm{sol}}$ (kg h$^{-1}$) | $w_{CO2}$ kg / kg | Reynolds number (solution) | Particle diameter $\mu$m |
|---|---|---|---|---|---|---|---|---|---|
| 1 | 1mm | 308 | 90 | 750 | 3 | 0.34 | 90 | 2400 | 80 |
| 2 | 1mm | 308 | 90 | 1500 | 3 | 0.34 | 90 | 2400 | 100 |
| 3 | 100$\mu$m | 308 | 100 | 750 | 3 | 0.34 | 90 | 24,000 | 8 |
| 4 | 100$\mu$m | 308 | 100 | 750 | 3 | 0.68 | 85 | 48,000 | 20 |
| 5 | 100$\mu$m | 308 | 100 | 750 | 4 | 0.25 | 94 | 17,000 | 8 |
| 6 | 100$\mu$m | 308 | 100 | 350 | 3 | 0.34 | 94 | 24,000 | 23 |

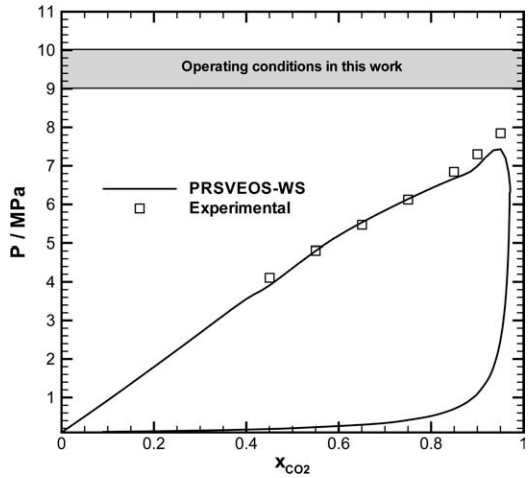


**Figure 2. $C_\phi$ dependence with $Re_L$ and Sc.**

commercial code employed was ANSYS FLUENT v.12.0.16. An special care was given to the grid model of the 100$\mu$m nozzle since the assumption of continuum hypothesis is compulsory to produce accurate results from Navier-Stokes equations.

## Results and Discussion

In this section, the main results obtained from the model are presented and analyzed. First, the experimental validation of the model is discussed. Then the flow field analysis and the results related to mixing dynamics within the precipitator are reported. Finally, the influence of different parameters pertaining to the model is commented.

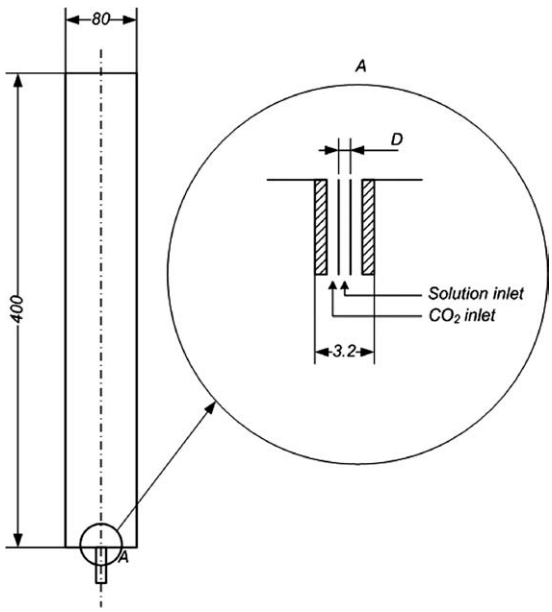


**Figure 3. Computational domain employed in this work. Dimensions are in milimeters. The diameter of the solution nozzle *D* is taken to be equal to 1 or 0.1 mm.**

**Table 2. Experimental ($d_p$) and Calculated ($d_{43}$) particle diameters, $\sigma = 0.008$ N m$^{-1}$**

| Case | Experimental $d_p$ $\mu$m | Calculated $d_{43}$ $\mu$m |
|---|---|---|
| 1 | 80 | 76 |
| 2 | 100 | 90 |
| 3 | 8 | 6 |
| 4 | 20 | 15 |
| 5 | 8 | 23 |
| 6 | 23 | 13 |

### *Experimental validation*

Validation is necessary to use the model with confidence. Therefore, it is necessary to compare the model predictions with experimental results to reduce the uncertainty of the calculations.

By using the data set presented above as boundary conditions, the results shown in Table 2 are obtained. Mean particle size is reported here in terms of $d_{43}$, namely the ratio between $\widetilde{M}^4$ and $\widetilde{M}^3$:

$$d_{43} = \frac{\widetilde{\mathcal{M}^4}}{\widetilde{\mathcal{M}^3}}. \tag{38}$$

It is necessary to note that most of the model parameters are known and easily derived from the theory, but the value of the surface solid-fluid tension is unknown. Different values were tested and eventually the value of 0.008 N m$^{-1}$ resulted in the best agreement with the experimental data obtained under different operating conditions. Table 2 compares the predictions with the experimental data.

Closer inspection of Table 2 shows that the model predicts the experimental trend for the mean particle size: Cases 1 and 2 correspond to simulation runs with the 1mm nozzle. The values obtained by fixing $\sigma = 0.008$ N m$^{-1}$ are very similar to those of the experiments. A similar behavior is found in Cases 3 to 6, corresponding to the 100 $\mu$m nozzle. The agreement between model predictions and experimental

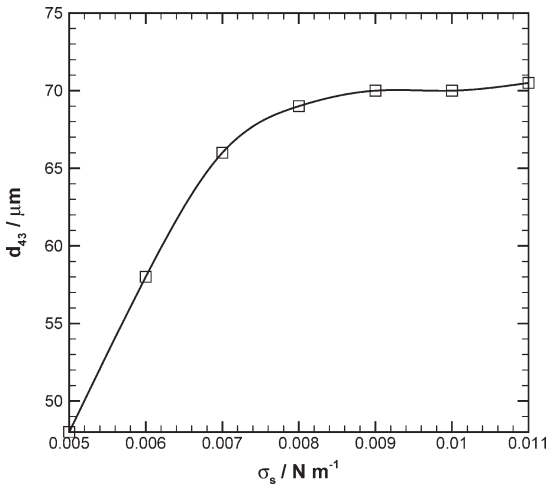


**Figure 4. Surface tension effect on the final particle size.**

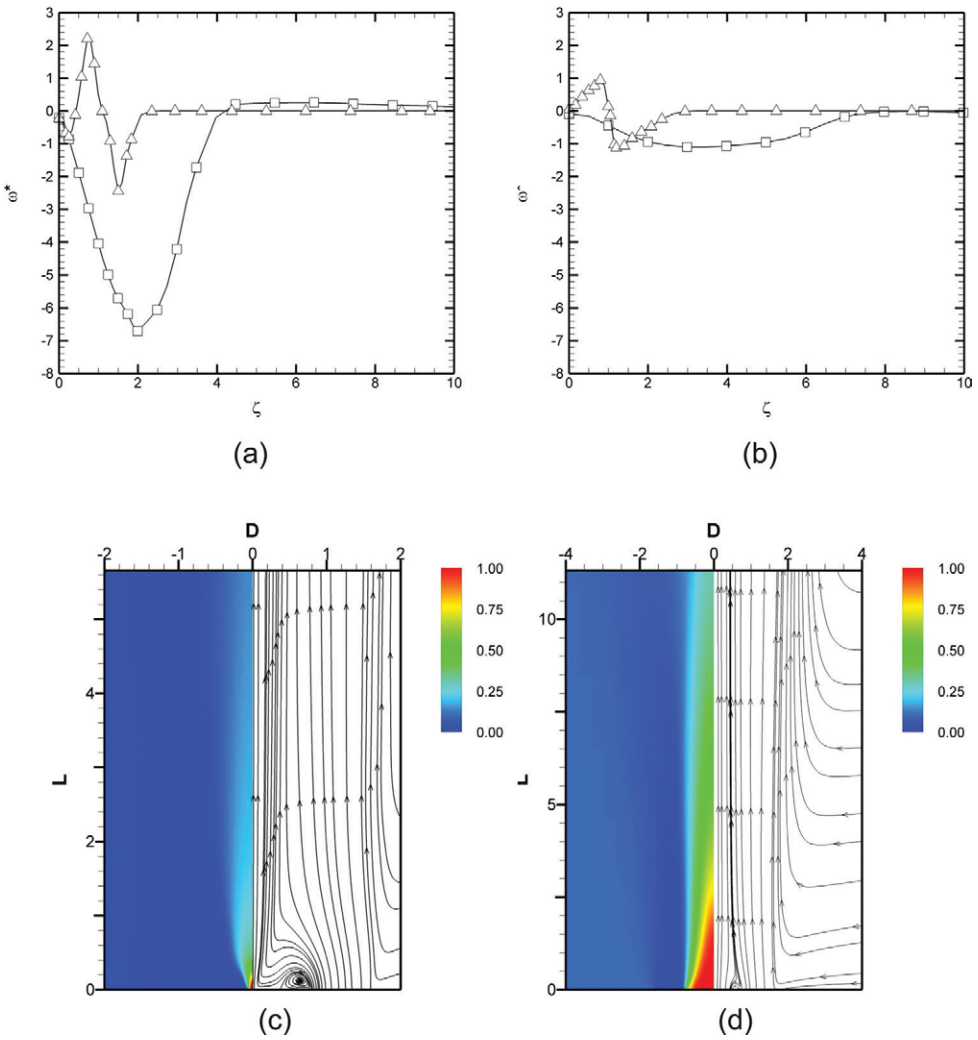


**Figure 5. (a) and (b) correspond to dimensionless vorticity at different heights from the nozzle in the precipitator at 1 mm and 5 mm, respectively. Triangles correspond to the 1 mm nozzle (Case 1) and squares correspond to the 100 $\mu$m nozzle (Case 4). (c) and (d) are countour plots of mixture fraction and streamlines close the nozzle, c) corresponds to the 100 $\mu$m nozzle (Case 4) and (d) corresponds to the 1mm nozzle (Case 1). Dimensions *D* and *L* mean radial and axial, respectively, in mm.**

[Color figure can be viewed in the online issue, which is available at wileyonlinelibrary.com.]

data validates the proposed model. Concluding, it is interesting to note that the value of the surface tension used in this work is consistent with that found by other authors for similar systems.[9]

Figure 4 shows the effect of the value of surface tension on the final particle size for one sample case related to the 1 mm nozzle. As it is shown, the lower the value of the surface tension the lower the particle size. This is mainly due to the strong dependence of the nucleation rate with this parameter. Smaller values of $\sigma$ lead to higher nucleation rates, which necessarily imply smaller particle sizes.

### *Flow field*

In this section, the different macromixing mechanisms associated with the nozzles analyzed are discussed. In the experimental device, the solution containing the solute (i. e., $\beta$ - carotene) and $CO_2$ enter by separate ducts and are coaxially mixed, generating the mixing layer. Because of the enormous difference in diameter between the precipitation chamber and the nozzle, the overall flow pattern is that of a backward facing step: part of the fluid moving downwards recirculates due to backmixing and mix again with the fresh feed.

To compare the results of both nozzles, the dimensionless vorticity is plotted against the normalized radial distance. The definition of these two variables is respectively:

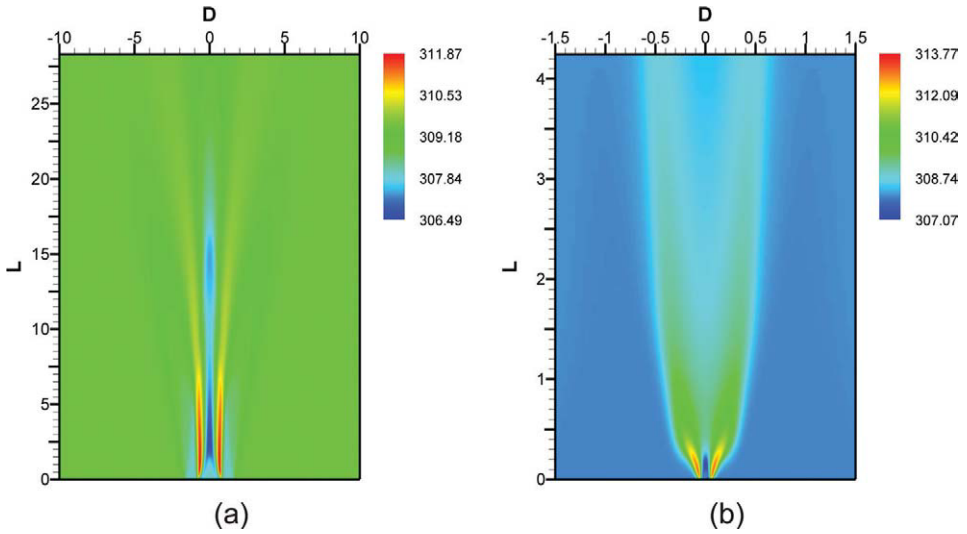


**Figure 6. Local temperature in the precipitation chamber (K).**

(a) 1 mm nozzle (Case 1); (b) 100 $\mu$m nozzle (Case 4). Dimensions $D$ and $L$ mean radial and axial, respectively, in mm. [Color figure can be viewed in the online issue, which is available at wileyonlinelibrary.com.]

$$\omega^{\star} = \frac{\omega L}{U}, \qquad \zeta = \frac{r}{D}, \tag{39}$$

where $r$ is the radius of the precipitator; $D$ is the diameter of the nozzle, $\omega$ is the vorticity; $L$ is a characteristic dimension and $U$ is a characteristic velocity. In this case, $L$ is taken equal to the value of the internal diameter of the $CO_2$ pipe (a common value in both geometries) and $U$ is equal to the average velocity of injection of the solution in each case. The results at different distances from the nozzle on the axis of the vessel are shown in Figures 5a,b.

The solution injection velocity determines the flow pattern near the nozzle, and the formation of vortices responsible for mixing at the macroscale. In the figure, the center of the vortices corresponds to the maximum and minimum values of vorticity. With the 1 mm nozzle, the injection velocity of the solution is lower than the $CO_2$ injection velocity. Two counter - rotating vortices attached to the wall are created. These eddies retain their identity up to 15 mm away from the nozzle. In the 100 $\mu$m nozzle, the injection velocity of the solution jet is much higher than $CO_2$, so the flow pattern associated with this nozzle is completely different (since the Reynolds number is one order of magnitude higher). The solution jet generates one strong vortex that promotes macromixing intensely and, as shown in the figure, this vortex convects fluid from one inlet to the other much faster than in the other case. This behavior is also noticeable in Figures 5c,d, that show contour plots of the mixture fraction and streamlines close to the nozzles.

Figure 6 shows the temperature contours calculated with the model for the two cases discussed. The effect of mixing of the solution with the $CO_2$ stream is evident. In the mixing layer temperature differs up to 4°C in relation to the final temperature of the fluid observed, although in the case of the 100 $\mu$m nozzle, the temperature is homogenized faster and the gradient is better localized.

### *Mixing dynamics*

In this section, mixing in the different devices under different operating conditions are analyzed in terms of the mean mixture fraction and the mixture fraction variance. Figure 7 shows the contours of mixture fraction and mixture fraction variance predicted by the model for both nozzles.

As already reported, each flow pattern completely determines mixing at all scales. In the 1 mm nozzle (Figure 7a) because mixing occurs slowly, mixture fraction gradients endure in the precipitator up to 50 mm downstream. Besides, due to the low injection velocity, the value of the local Reynolds number is not large. Because of the persistence of the gradients and in conjunction with the low value of the local Reynolds number, microsegregated regions (identified by high values of the mixture fraction variance) are extended up to 14 mm beyond the nozzle.

The same explanation applies to Figure 7b, which shows the variance contour for the 100 $\mu$m nozzle. It must be emphasized here that however, in this case, the area where mixture fraction variance is larger than zero is much smaller than for the 1 mm nozzle. This is because the local Reynolds number is higher due to the increased injection velocity, although the variance generation rate is very high, since the mixture fraction gradient is also very high. Furthermore, its decay rate is also large due to the high value of the local Reynolds number. The combination of these two phenomena makes mixing faster and efficient in this configuration and under these operating conditions.

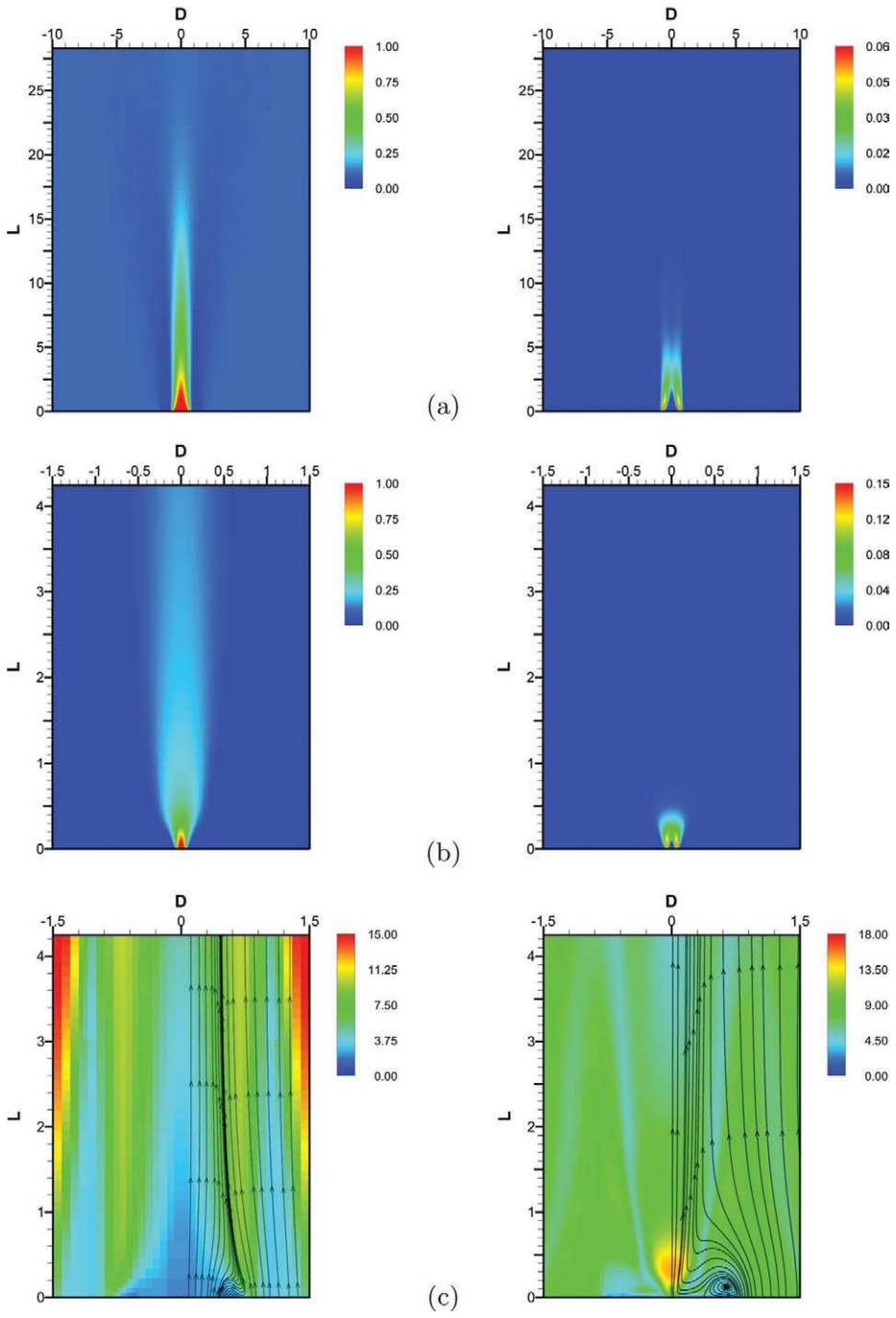


**Figure 7. Mixture fraction contours (left) and mixture fraction variance contours (right).**

(a) 1 mm nozzle (Case 1); (b) 100 $\mu$m nozzle (Case 4); (c) Local Reynolds value, left:1mm nozzle, right:100 $\mu$m nozzle. Dimensions $D$ and $L$ mean radial and axial, respectively, in mm. [Color figure can be viewed in the online issue, which is available at wileyonlinelibrary.com.]

### *Particle diameter prediction*

Figures 8 and 9 show the contours of particle number density (i. e., $M^0$), supersaturation, nucleation rate and growth rate in the precipitator. High supersaturations cause high nucleation rates and therefore a large number of particles. Although for both mixers supersaturation reaches similar values, the number density is one order of magnitude higher with the 100 $\mu$m nozzle. There are various phenomena that are directly involved in the explanation of this behavior. The nucleation and growth rates are strong functions of supersaturation and when the fluid injection is relatively slow (such as in the case of the nozzle of 1 mm) the residence time in the mixing layer is higher and this is where most of the

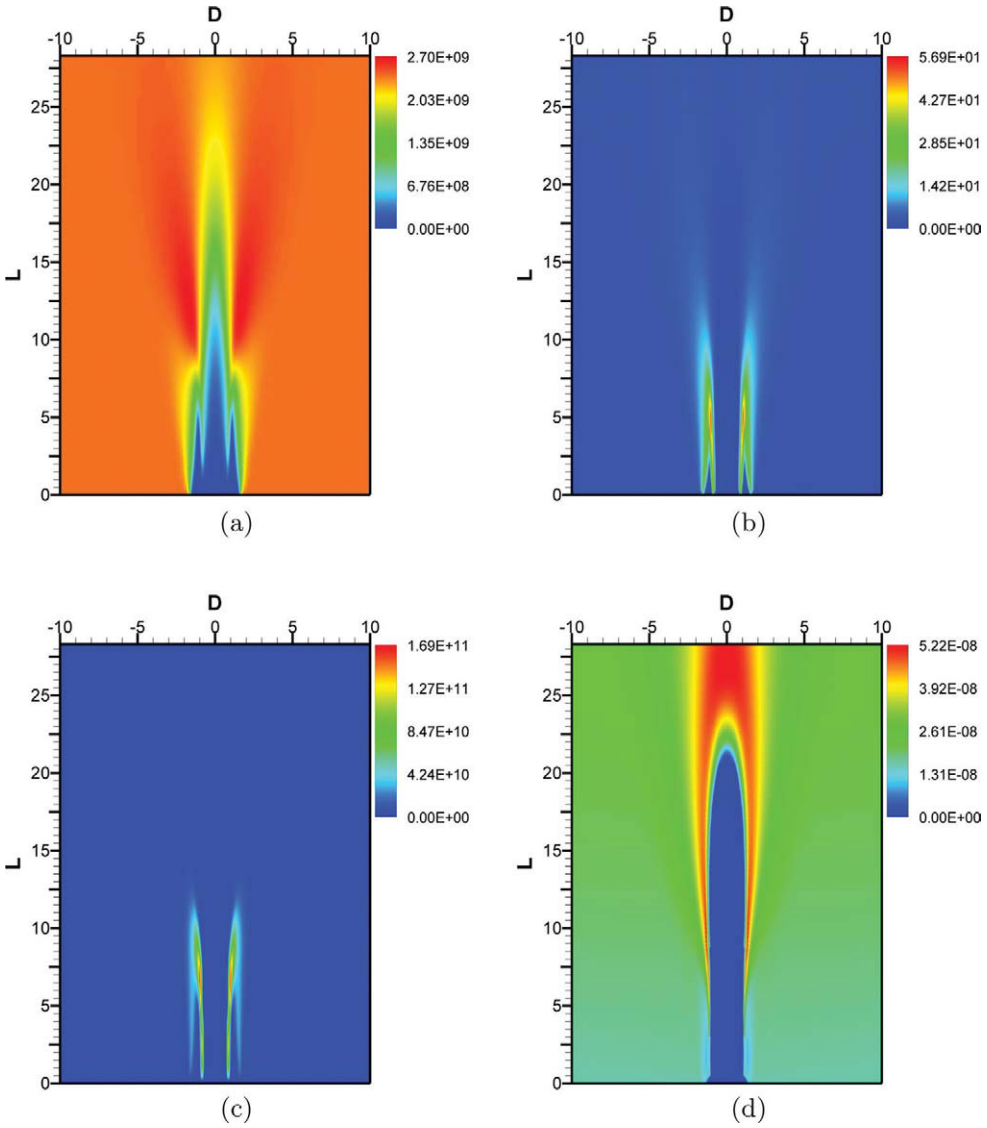


**Figure 8. (a) Number of particles inside the precipitator, (# $m^{-3}$). (b) Supersaturation. (c) Nucleation rate (# $m^{-3}$ $s^{-1}$). (d) Growth rate (m $s^{-1}$). Case 1, 1 mm nozzle. Dimensions *D* and *L* mean radial and axial, respectively, in mm.**

[Color figure can be viewed in the online issue, which is available at wileyonlinelibrary.com.]

supersaturation is spatially accumulated. Regarding outlet supersaturation, it is close to six for both geometries.

The contours of calculated supersaturation with the 1mm nozzle show an interesting effect: there is a double reacting layer. First, the solution comes into contact with $CO_2$ in the mixing layer, where the particles begin to precipitate. However, the precipitation process is not complete, so the ready-mixed fluid moves downstream with still a certain amount of unprecipitated $\beta$- carotene. Due to the overall flow pattern in the precipitator, part of the fluid is recirculated back into the nozzle, which re-establishes a front of precipitation with high supersaturation. This effect is not observed with the 100 $\mu$m nozzle (see Figure 8), where it seems that the recirculated fluid does not have a sufficient amount of solute to generate high supersaturation during backmixing.

When the fluid injection takes place at a faster rate, particles do not have enough time to grow and the particle number density is higher. Furthermore, the high supersaturation region is larger than in the previous case. This is confirmed by Figure 10 that presents the mean particle size in the precipitator for the two nozzles.

The importance of the effect of aggregation in this system has been assesed by disabling the corresponding source terms in the moment transport equations. Results show that in cases where the final particle size is smaller, aggregation does not play an important role, while on the contrary, it does when large particles are formed. For instance, in Cases 1 and 2 if aggregation was neglected model predictions would have resulted in 59 and 80 $\mu$m respectively, with a significant disagreement with experiments. Although in the other analyzed cases differences

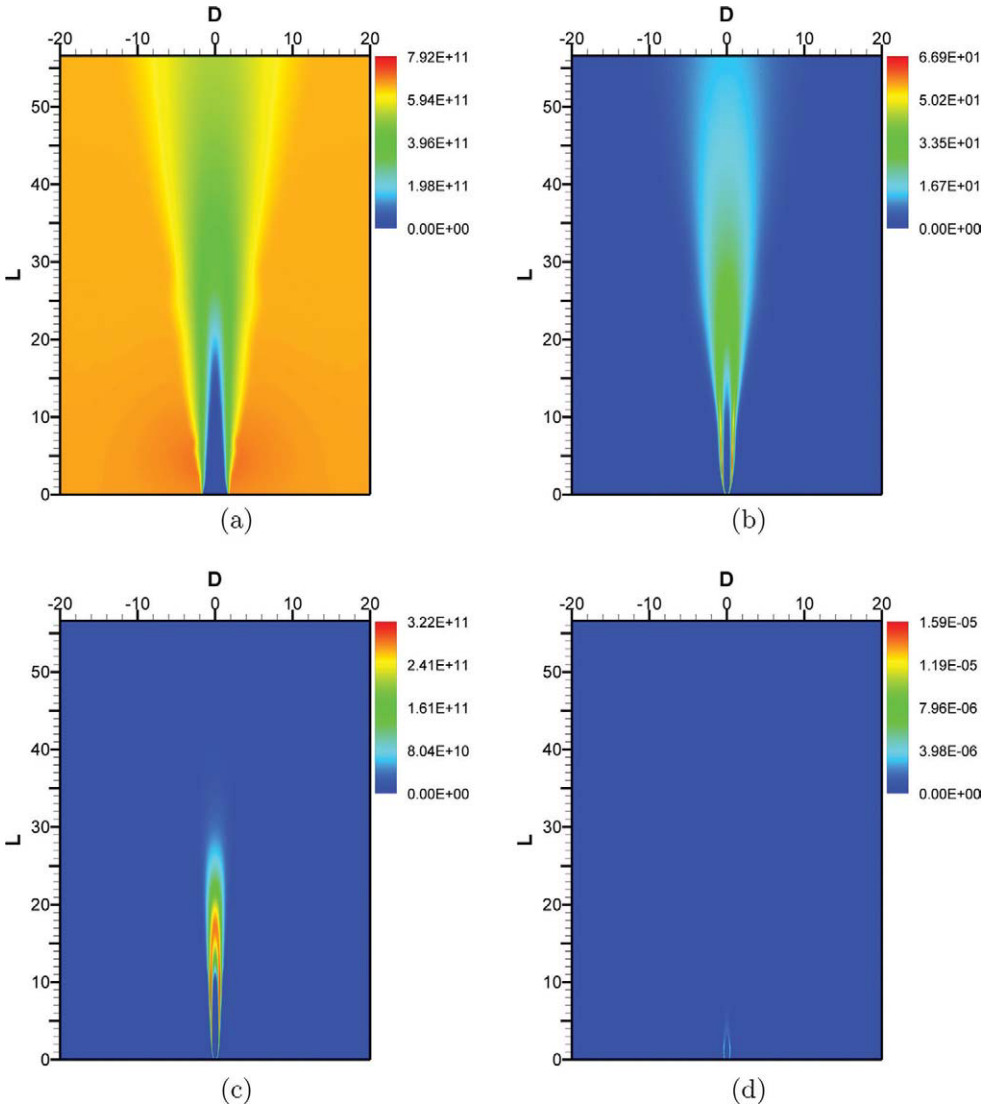


**Figure 9. (a) Number of particles inside the precipitator, (# $m^{-3}$). (b) Supersaturation. (c) Nucleation rate (# $m^{-3}$ $s^{-1}$). (d) Growth rate (m $s^{-1}$). Case 4, 100 $\mu$m nozzle. Dimensions *D* and *L* mean radial and axial, respectively, in mm.**

[Color figure can be viewed in the online issue, which is available at wileyonlinelibrary.com.]

were less significant, aggregation seems to be important in interpreting the experiments.

### *Effects of micromixing on the final particle size*

To establish the importance of the micromixing model, calculations have been performed also by deactivating the micromixing submodel (i. e., DQMoM-IEM). Results show that in the case of the 100 $\mu$m nozzle, predictions are not significantly affected by the micromixing model, probably because under these conditions mixing is very fast. However, there is a significant effect in the case of the 1 mm nozzle, where mixing is much slower: Cases 1 and 2 present lower particle sizes when the micromixing model is not activated (32 and 40 $\mu$m, respectively).

## Conclusions

A model to describe precipitation of $\beta$- carotene using the SAS process has been developed. This model includes submodels of mixing (DQMoM-IEM) and precipitation (QMoM), for analyzing phenomena associated with mixing within the precipitator. Different nozzles have been tested and the results obtained with the model have been validated against experimental data. The predictions match well with experimentals in all the cases studied. Although, due to the lack of knowledge of a simple model parameter

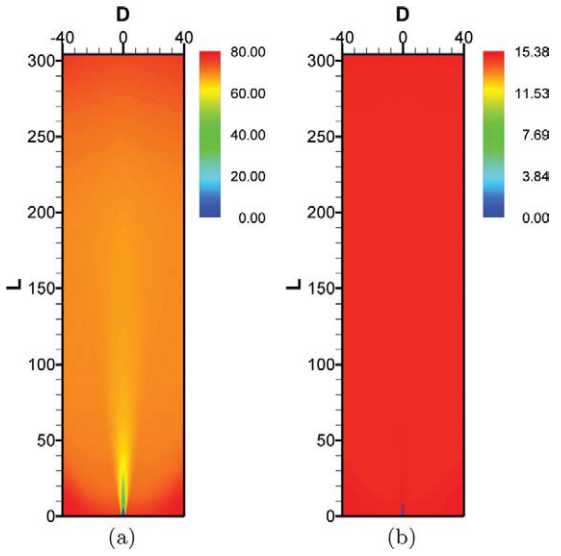


**Figure 10. Particle diameter $d_{43}$. (a) 1 mm nozzle (Case 1); (b) 100 $\mu$m nozzle (Case 4). Dimensions *D* and *L* mean radial and axial, respectively, in mm.**

[Color figure can be viewed in the online issue, which is available at wileyonlinelibrary.com.]

the model cannot be used in a total predictive way, through a fitting procedure this parameter was successfully identified. The final model seems to be able to explain the experimental trend in terms of the competition between nucleation, growth, and aggregation and offers a valuable insight into the process.

The next steps of this work will be in the direction of a further validation of the model in a wider range of operating conditions. In particular, those cases in which mixing highly affects precipitation will be further investigated. A follow up of this study will instead examine the optimum range of Reynolds number for each geometry in which turbulence effects can be avoided resulting in a final product with optimum quality

## Acknowledgments

Authors thank Junta de Castilla y León, Project Reference: GR11 - 2008 and to the Grant-in-Aid for the Research Group of Excellence GR57 - Engineering of the Fluids for financial support.

## Literature Cited

1. Jung J, Perrut M. Particle design using supercritical fluids: Literature and patent survey. *J Supercrit Fluids.* 2001;20:179–219.
2. Reverchon E, Adami R. Nanomaterials and supercritical fluids. *J Supercrit Fluids.* 2006;37:1–22.
3. Martín A, Cocero M. Micronization processes with supercritical fluids: Fundamentals and mechanisms. *Adv Drug Delivery Rev.* 2008;60:339–350.
4. Baldyga J, Kubicki D, Shekunov BY, Smith KB. Mixing effects on particle formation in supercritical fluids. *Chem Eng Res Des.* 2010; 88:1131–1141.
5. Baldyga J, Makowski L, Orciuch W. Interaction between mixing, chemical reactions, and precipitation. *Ind Eng Chem Res.* 2005;44:5342–5352.
6. Shekunov BY, Baldyga J, York P. Particle formation by mixing with supercritical antisolvent at high Reynolds numbers. *Chem Eng Sci.* 2001;56:2421–2433.
7. Werling J, Debenedetti P. Numerical modeling of mass transfer in the supercritical antisolvent process: miscible conditions. *J Supercrit Fluids.* 2000;18:11–24.
8. Chavez F, Debenedetti P, Luo J, Dave R, Pfeffer R. Estimation of the characteristic time scales in the supercritical antisolvent process. *Ind Eng Chem Res.* 2003;42:3156–3162.
9. Martín A, Cocero MJ. Numerical modeling of jet hydrodynamics, mass transfer and crystallization kinetics in the supercritical antisolvent (SAS) process. *J Supercritical Fluids.* 2004;32:203–219.
10. Pratsinis SE. Simultaneous nucleation, condensation, and coagulation in aerosol reactors. *J Colloid Interface Sci.* 1988;124:416–427.
11. Henczka M, Baldyga J, Shekunov B. Particle formation by turbulent mixing with supercritical antisolvent. *Chem Eng Sci.* 2005;60:2193–2201.
12. Baldyga J. Turbulent mixer model with application to homogeneous, instantaneous chemical reactions. *Chem Eng Sci.* 1989;44:1175–82.
13. Oschwald M, Smith JJ, Branam R, Hussong J, Schik A, Chehroudi B, Talley D. Injection of fluids into supercritical environments. *Combust Sci Technol.* 2006;178:49–100.
14. Stryjek R, Vera JH. PRSV: An improved Peng-Robinson equation of state for pure compounds and mixtures. *Can J Chem Eng.* 1986;64:323–333.
15. Kikic I, Lora M, Bertucco A. A thermodynamic analysis of three-phase equilibria in binary and ternary systems for applications in rapid expansion of a supercritical solution (RESS), particles from gas-saturated solutions (PGSS), and supercritical antisolvent (SAS). *Ind Eng Chem Res.* 1997;36:5507–5515.
16. Sierra-Pallares J, Alonso E, Montequi I, Cocero M. Particle diameter prediction in supercritical nanoparticle synthesis using three-dimensional CFD simulations. Validation for anatase titanium dioxide production. *Chem Eng Sci.* 2009;64:3051–3059.
17. Wong D, Sandler S. A theoretically correct mixing rule for cubic equations of state. *AIChE J.* 1992;38:671–680.
18. Orbey H, Sandler SI. A comparison of various cubic equation of state mixing rules for the simultaneous description of excess enthalpies and vapor-liquid equilibria. *Fluid Phase Equilib.* 1996;121:67–83.
19. Escobedo-Alvarado G, Sandler S. Prediction of Excess Enthalpies Using a Gex/EOS Model. *Ind Eng Chem Res.* 2001;40:1261–1270.
20. Renon H, Prausnitz J. Local compositions in thermodynamic excess functions for liquid mixtures. *AIChE J.* 1968;14:135–144.
21. Orbey H, Sandler S. *Modeling vapor-liquid equilibria: Cubic equations of state and their mixing rules.* Cambridge, UK: Cambridge University Press. 1998.
22. Meng H, Yang V. A unified treatment of general fluid thermodynamics and its application to a preconditioning scheme. *J Comput Phys.* 2003;189:277–304.
23. Anderson D, Tannehill J, Pletcher R. *Computational Fluid Mechanics and Heat Transfer*. Hemisphere, Washington, DC. 1984.
24. Shih T, Liou W, Shabbir A, Yang Z. A new k-$\epsilon$ eddy viscosity model for high Reynolds number turbulent flows. *Comput Fluids.* 1995;24:227–227.
25. Sierra-Pallares J, Parra-Santos M, García-Serna J, Castro F, Cocero M. Numerical analysis of high-pressure fluid jets: Application to RTD prediction in supercritical reactors. *J Supercrit Fluids.* 2009;49:249–255.
26. Dirksen J, Ring T. Fundamentals of crystallization: kinetic effects on particle size distributions and morphology. *Cheml Eng Sci.* 1991;46:2389–2427.
27. Marchisio D, Soos M, Sefcik J, Morbidelli M, Barresi A, Baldi G. Effect of fluid dynamics on particle size distribution in particulate processes. *Chem Eng Technol.* 2006;29:191–199.
28. Liu Y, Fox R. CFD predictions for chemical processing in a confined impinging-jets reactor. *AIChE J.* 2006;52:731–744.
29. Gavi E, Marchisio D, Barresi A. CFD modelling and scale-up of Confined Impinging Jet Reactors. *Chem Eng Sci.* 2007;62:2228–2241.
30. Fox R. *Computational models for turbulent reacting flows.* Cambridge, UK: Cambridge University Press. 2003.
31. Corrsin S. The isotropic turbulent mixer: Part II. Arbitrary Schmidt number. *AIChE J.* 1964;10:870–877.
32. Marchisio D, Pikturna J, Fox R, Vigil R, Barresi A. Quadrature method of moments for population-balance equations. *AIChE J.* 2003;49:1266–1276.

33. McGraw R. Description of aerosol dynamics by the quadrature method of moments. *Aerosol Sci Technol*. 1997;27:255–265.
34. Debenedetti P, Tom J, Sang-Do Y, Gio-Bin L. Application of supercritical fluids for the production of sustained delivery devices. *J Controlled Release*. 1993;24:27–44.
35. Dixon D, Johnston K. Molecular thermodynamics of solubilities in gas antisolvent crystallization. *AIChE J*. 1991;37:1441–1449.
36. Escobedo-Alvarado G, Sandler S, Scurto A. Modeling of solid–supercritical fluid phase equilibria with a cubic equation of state – $G^{ex}$ model. *J Supercrit Fluids*. 2001;21:123–134.
37. Gavi E. Investigation of turbulent precipitation of nanoparticles in a confined impinging-jets reactor. Ph.D. thesis, Politecnico di Torino (Italy). Dipartimento di Scienza Materiali e Ingegnieria Chimica. 2009.
38. Mersmann A. *Crystallization technology handbook*. New York: Marcel Dekker Inc. 2001.
39. Batchelor G. Mass transfer from small particles suspended in turbulent fluid. *J Fluid Mechs*. 1980;98:609–623.
40. Armenante P, Kirwan D. Mass transfer to microparticles in agitated systems. *Chem Eng Sci*. 1989;44:2781–2796.
41. Chung T, Ajlan M, Lee L, Starling K. Generalized multiparameter correlation for nonpolar and polar fluid transport properties. *Ind Eng Chem Res*. 1988;27:671–679.
42. He C, Yu Y. New equation for infinite-dilution diffusion coefficients in supercritical and high-temperature liquid solvents. *Ind Eng Chem Res*. 1998;37:3793–3798.
43. Cocero MJ, Ferrero S, Miguel F. *Crystallization of β-carotene by continuous gas process. Effect of mixer on crystals formation*. In: *4th International symposium on high pressure process technology and chemical engineering*. Venice, Italy, 2002.
44. Miguel F, Martin A, Gamse T, Cocero M. Supercritical anti solvent precipitation of lycopene:: Effect of the operating parameters. *J Supercrit Fluids*. 2006;36:225–235.
45. Martin A, Mattea F, Gutierrez L, Miguel F, Cocero M. Co-precipitation of carotenoids and bio-polymers with the supercritical anti-solvent process. *J Supercrit Fluids*. 2007;41:138–147.
46. Miguel F, Martin A, Mattea F, Cocero M. Precipitation of lutein and co-precipitation of lutein and poly-lactic acid with the supercritical anti-solvent process. *Chem Eng Process: Process Intensification*. 2008;47:1594–1602.
47. Gonzalez A, Tufeu R, Subra P. High-Pressure Vapor– Liquid Equilibrium for the Binary Systems Carbon Dioxide+ Dimethyl Sulfoxide and Carbon Dioxide+ Dichloromethane. *J Chem Eng Data*. 2002;47:492–495.

*Manuscript received Jun. 2, 2010, and revision received Jan. 13, 2011.*